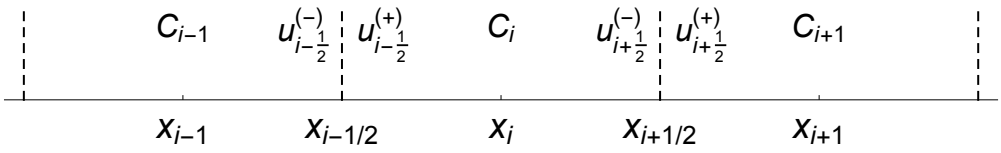

Fig. 1. Stencil for reconstruction of interface values on equidistant grids, i.e. $\Delta x_i = x_{i+\frac{1}{2}} - x_{i-\frac{1}{2}} \equiv \Delta x \; \forall i$.

on their work, Čada and Torrilhon developed a third-order limiter function avoiding the above-mentioned extrema clipping. Our recent article [19] continued this work, introducing a third-order limiter function $H^{(c)}_{3L}$. This function contains a decision criterion able to distinguish between smooth extrema and discontinuities. This limiter was first developed and tested for one-dimensional hyperbolic conservation laws on uniform grids in the context of finite volume methods. Now, the aim is to extend the scheme to make it applicable for numerical test cases on non-uniform meshes and in two space dimensions.

The paper is structured as follows: in Sec. 2 we recall the formulation of the third-order limiter function $H^{(c)}_{3L}$ in one space dimension for equidistant grids. Then, the limiter is extended for the use of non-equidistant grids. Sec. 3 explains the extension to two space dimensions and the order-fix which allows to maintain high-order accuracy within the flux-splitting framework. Here, we firstly treat Cartesian grids in Sec. 3.1, then introduce a parallel adaptive-mesh-refinement (AMR) framework in Sec. 3.2, and in Sec. 3.3 extend the theory of non-uniform grids to two space dimensions. Numerical results visualizing the theoretical concepts are presented in Sec. 4 and in Sec. 5 we draw some conclusions. Finally, more details on the formulation of the limiter function on uniform as well as non-uniform grids can be found in the appendix.

2. Third-Order Limiter in One Space Dimension

Achieving high-order accuracy with finite volume schemes requires large stencils. This leads to an increase in communication among grid cells and is undesirable when thinking of parallel codes and boundaries. Therefore, we want to remain on the most compact stencil of three cells in one-dimension and five cells in two space dimensions. This means, the stencil consists of the cell of interest and its direct neighbors.

For the sake of simplicity, we restrict the theoretical development of the limiter function to one dimensional scalar equations. The transition from the one-dimensional formulation to two-dimensions is obtained via a dimensional splitting. The exact procedure is explained in Sec. 3. Also, the theory easily extends to systems of conservation laws by applying it component-wise.

In the one-dimensional case of Cartesian grids, we divide the domain of interest $\Omega \subset \mathbb{R}$ in non-overlapping cells $C_i = [x_{i-\frac{1}{2}}, x_{i+\frac{1}{2}})$ such that $\Omega = \bigcup_i C_i$. Denote by x_i the cell centers and by $\Delta x_i = x_{i+\frac{1}{2}} - x_{i-\frac{1}{2}}$ the size of cell C_i. Fig. 1 depicts the here-introduced notation for the equidistant case $\Delta x_i \equiv \Delta x \; \forall i$.

In this work we are interested in hyperbolic conservation law of the form

$$\partial_t u(\boldsymbol{x}, t) + \nabla \cdot f(u(\boldsymbol{x}, t)) = 0 \tag{2.1}$$

with suitable initial conditions $u(\boldsymbol{x}, 0) = u_0(\boldsymbol{x})$, $\boldsymbol{x} = x$ in 1D and $\boldsymbol{x} = (x, y)^T$ in 2D, respectively. To avoid boundary effects, we impose periodic boundary conditions. Integrating Eq. (2.1) in one space dimension over cell C_i and dividing by the cell width Δx_i yields an exact update formula for the cell mean values $\frac{1}{\Delta x_i}\int_{C_i} u(x,t)dx$. This formulation however requires the exact solution of Riemann problems at each cell boundary [15]. To avoid this costly procedure, approximate Riemann solvers are incorporated and the exact cell mean values are approximated by $\bar{u}_i$. The update formula for $\bar{u}_i$ is then given by the so-called semi-discrete scheme

$$\frac{d\,\bar{u}_i}{d\,t} = -\frac{1}{\Delta x_i}\left(\hat{f}_{i+\frac{1}{2}} - \hat{f}_{i-\frac{1}{2}}\right), \tag{2.2}$$

with numerical flux functions $\hat{f}_{i+\frac{1}{2}} = \hat{f}(u^{(-)}_{i+\frac{1}{2}}, u^{(+)}_{i+\frac{1}{2}})$ and $\hat{f}_{i-\frac{1}{2}} = \hat{f}(u^{(-)}_{i-\frac{1}{2}}, u^{(+)}_{i-\frac{1}{2}})$. These functions take as input the left and right limiting values at the cell interface, see Fig. 1. One could simply insert the left and right

cell mean values, however, this only yields a first-order accurate scheme [15]. In order to achieve higher-order accuracy, one way is to use reconstructions for the interface values. As described in more detail in [19], the reconstructed interface values of cell i can be written in the general form

$$u_{i+\frac{1}{2}}^{(-)} = \bar{u}_i + \tfrac{1}{2}\, H(\delta_{i-\frac{1}{2}}, \delta_{i+\frac{1}{2}}) = M(\bar{u}_{i-1}, \bar{u}_i, \bar{u}_{i+1}), \tag{2.3a}$$

$$u_{i-\frac{1}{2}}^{(+)} = \bar{u}_i - \tfrac{1}{2}\, H(\delta_{i+\frac{1}{2}}, \delta_{i-\frac{1}{2}}) = P(\bar{u}_{i-1}, \bar{u}_i, \bar{u}_{i+1}). \tag{2.3b}$$

The function H fully determines the way limiting is performed and thus the order of accuracy of the resulting scheme. The undivided differences between neighboring cells are denoted by

$$\begin{aligned} \delta_{i-\frac{1}{2}} &= \bar{u}_i - \bar{u}_{i-1} \\ \delta_{i+\frac{1}{2}} &= \bar{u}_{i+1} - \bar{u}_i. \end{aligned} \tag{2.4}$$

Remark:. The standard form for reconstructions, e.g. found in [15] reads

$$u_{i+\frac{1}{2}}^{(-)} = \bar{u}_i + \tfrac{1}{2}\, \phi(\theta_i)\delta_{i-\frac{1}{2}}, \tag{2.5a}$$

$$u_{i-\frac{1}{2}}^{(+)} = \bar{u}_i - \tfrac{1}{2}\, \phi(\theta_i^{-1})\delta_{i+\frac{1}{2}} \tag{2.5b}$$

with the ratio of consecutive gradients $\theta_i = \delta_{i-\frac{1}{2}}/\delta_{i+\frac{1}{2}}$ which acts as a smoothness indicator and a monovariant limiter function ϕ. This form, introduced by [5, 8] relates to Eq. (2.3) via $\phi(\theta_i)\delta_{i-\frac{1}{2}} = H(\delta_{i-\frac{1}{2}}, \delta_{i+\frac{1}{2}})$. More details on the two-variate form and its advantages can be found in [19].

2.1. Formulation for Equidistant Grids

In this section we will shortly recall the formulation of third-order limiter functions for equidistant grids developed in [19].

Starting with a quadratic ansatz function, evaluated on $(x_{i-1}, \bar{u}_{i-1}), (x_i, \bar{u}_i), (x_{i+1}, \bar{u}_{i+1})$, we can obtain an unlimited reconstruction formulation which yields a third-order accurate scheme. Rewriting the polynomial reconstruction in the form (2.3) yields

$$u_{i\pm\frac{1}{2}}^{(\mp)} = \bar{u}_i \pm \frac{1}{2}\, \frac{\delta_{i+\frac{1}{2}} + \delta_{i\pm\frac{1}{2}} + \delta_{i-\frac{1}{2}}}{3} \tag{2.6}$$

leading to the function

$$H_3(\delta_{i-\frac{1}{2}}, \delta_{i+\frac{1}{2}}) := \frac{1}{3}\left(2\delta_{i+\frac{1}{2}} + \delta_{i-\frac{1}{2}}\right). \tag{2.7}$$

For purely smooth functions, the full (unlimited) third-order reconstruction shows good results. However, for solutions containing discontinuities, spurious oscillations develop since a linear higher-order method is not monotonicity preserving [15]. Therefore, we need to apply non-linear reconstruction functions. In [19] we recently constructed a limiter function, called $H_{3\mathrm{L}}$, based on a double logarithmic ansatz function, first proposed by Artebrant and Schroll [1] and further developed by Čada and Torillhon [5]. Furthermore, we designed the combined limiter function $H_{3\mathrm{L}}^{(c)}$ which includes a decision criterion $\eta = \eta(\delta_{i-\frac{1}{2}}, \delta_{i+\frac{1}{2}})$, able to distinguish between smooth extrema and discontinuities. The combined limiter applies the full third-order reconstruction H_3 on parts which are classified as smooth and switches to the limited function $H_{3\mathrm{L}}$ if η indicates large gradients. It reads

$$H_{3\mathrm{L}}^{(c)}(\delta_{i-\frac{1}{2}}, \delta_{i+\frac{1}{2}}) := \begin{cases} H_3(\delta_{i-\frac{1}{2}}, \delta_{i+\frac{1}{2}}) & \text{if } \eta(\delta_{i-\frac{1}{2}}, \delta_{i+\frac{1}{2}}) < 1 \\ H_{3\mathrm{L}}(\delta_{i-\frac{1}{2}}, \delta_{i+\frac{1}{2}}) & \text{if } \eta(\delta_{i-\frac{1}{2}}, \delta_{i+\frac{1}{2}}) \geq 1. \end{cases} \tag{2.8}$$

The formulation for $H_{3\mathrm{L}}$ and the decision criterion η, as well as more details on $H_{3\mathrm{L}}^{(c)}$ are given in Appendix A.1 and in [19].

2.2. Formulation for Non-Equidistant Grids

For general grids, the size of cell C_i, denoted by Δx_i is not uniform for all cells, i.e. $\Delta x_i \neq \Delta x\ \forall i$, see Fig. 2. In this case, the definition of the undivided differences $\delta_{i\pm\frac{1}{2}}$ Eq. (2.4) is not meaningful anymore and new concepts need to be developed.

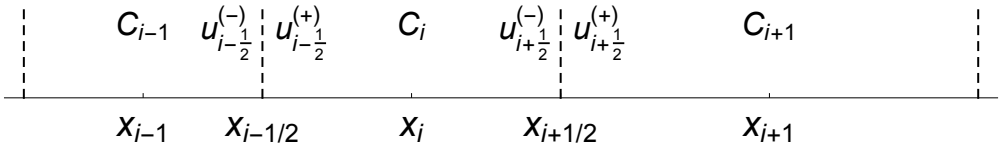

Fig. 2. Stencil for reconstruction of interface values in the non-equidistant case.

Starting again with the full third-order reconstruction, consider a quadratic polynomial $p_i(x)$ in cell i that has to maintain the cell averages in the three cells $C_{i+\ell},\ \ell \in \{-1, 0, 1\}$. This polynomial is then evaluated at the cell boundaries $x_{i\pm\frac{1}{2}}$ and yields the reconstructed cell interface values

$$u^{(-)}_{i+\frac{1}{2}} = p_i(x_{i+\frac{1}{2}}) \stackrel{!}{=} \bar{u}_i + \frac{1}{2} H_{3,\mathrm{neq}} \tag{2.9a}$$

$$u^{(+)}_{i-\frac{1}{2}} = p_i(x_{i-\frac{1}{2}}) \stackrel{!}{=} \bar{u}_i - \frac{1}{2} H_{3,\mathrm{neq}}. \tag{2.9b}$$

Even though this procedure is similar to the full third-order reconstruction on uniform grids, Eq. (2.7), the reconstruction function $H_{3,\mathrm{neq}}$ differs from H_3 since the different cell sizes need to be taken into account. The full (unlimited) third-order reconstruction function reads

$$H_{3,\mathrm{neq}}\left(\delta_{i-\frac{1}{2}}, \delta_{i+\frac{1}{2}}, \Delta x_i, \Delta x_{i-1}, \Delta x_{i+1}\right) = \frac{\Delta x_i}{\Delta_i} \frac{1}{3} \left(2 \frac{\Delta_{i-\frac{1}{2}}}{\Delta_{i+\frac{1}{2}}} \delta_{i+\frac{1}{2}} + \frac{\Delta x_{i+1}}{\Delta_{i-\frac{1}{2}}} \delta_{i-\frac{1}{2}} \right) \tag{2.10a}$$

with the abbreviations

$$\Delta_i = \frac{\Delta x_{i-1} + \Delta x_i + \Delta x_{i+1}}{3},\ \ \Delta_{i-\frac{1}{2}} = \frac{\Delta x_{i-1} + \Delta x_i}{2},\ \ \Delta_{i+\frac{1}{2}} = \frac{\Delta x_i + \Delta x_{i+1}}{2}. \tag{2.10b}$$

As in the equidistant case, the reconstructed interface values, Eq. (2.9), can be compactly refomulated as

$$u^{(\mp)}_{i\pm\frac{1}{2}} = \bar{u}_i \pm \frac{\Delta x_i}{2} \frac{\Delta x_{i-1} \widetilde{\delta}_{i+\frac{1}{2}} + \Delta x_i \widetilde{\delta}_{i\pm\frac{1}{2}} + \Delta x_{i+1} \widetilde{\delta}_{i-\frac{1}{2}}}{\Delta x_{i-1} + \Delta x_i + \Delta x_{i+1}} \tag{2.11a}$$

with

$$\widetilde{\delta}_{i-\frac{1}{2}} = \frac{\delta_{i-\frac{1}{2}}}{\Delta_{i-\frac{1}{2}}}, \qquad \widetilde{\delta}_{i+\frac{1}{2}} = \frac{\delta_{i+\frac{1}{2}}}{\Delta_{i+\frac{1}{2}}}. \tag{2.11b}$$

It can easily be seen that for equidistant grids, i.e. $\Delta x_{i-1} = \Delta x_i = \Delta x_{i+1} \equiv \Delta x$, the abbreviated terms reduce to $\Delta_i = \Delta_{i-\frac{1}{2}} = \Delta_{i+\frac{1}{2}} = \Delta x$ and therefore, the formulas for $H_{3,\mathrm{neq}}$ and H_3 match, as expected.

Eq. (2.10) and (2.11) indicate that for non-equidistant meshes, the equivalent of the undivided differences $\delta_{i\pm\frac{1}{2}}$ are the scaled slopes

$$u^{(-)}_{i+\frac{1}{2}}: \quad \begin{aligned} \delta_{i-\frac{1}{2}} \ &\rightarrow\ \Delta x_{i+1} \frac{\delta_{i-\frac{1}{2}}}{\Delta_{i-\frac{1}{2}}} = \Delta x_{i+1} \widetilde{\delta}_{i-\frac{1}{2}} \\ \delta_{i+\frac{1}{2}} \ &\rightarrow\ \Delta_{i-\frac{1}{2}} \frac{\delta_{i+\frac{1}{2}}}{\Delta_{i+\frac{1}{2}}} = \frac{\Delta x_i}{2} \widetilde{\delta}_{i+\frac{1}{2}} + \frac{\Delta x_{i-1}}{2} \widetilde{\delta}_{i+\frac{1}{2}} \end{aligned} \tag{2.12}$$

for the reconstruction of the right interface of cell C_i and

$$u^{(+)}_{i-\frac{1}{2}}: \quad \begin{aligned} \delta_{i-\frac{1}{2}} \ &\rightarrow\ \Delta_{i+\frac{1}{2}} \frac{\delta_{i-\frac{1}{2}}}{\Delta_{i-\frac{1}{2}}} = \frac{\Delta x_i}{2} \widetilde{\delta}_{i-\frac{1}{2}} + \frac{\Delta x_{i+1}}{2} \widetilde{\delta}_{i-\frac{1}{2}} \\ \delta_{i+\frac{1}{2}} \ &\rightarrow\ \Delta x_{i-1} \frac{\delta_{i+\frac{1}{2}}}{\Delta_{i+\frac{1}{2}}} = \Delta x_{i-1} \widetilde{\delta}_{i+\frac{1}{2}} \end{aligned} \tag{2.13}$$

for the reconstruction of the left interface of cell C_i. These expressions resemble the smoothness indicators introduced by Jiang and Shu [13], which are given by $\Delta x_i \widetilde{\delta}_{i-\frac{1}{2}}$ and $\Delta x_i \widetilde{\delta}_{i+\frac{1}{2}}$.

In order to generalize the third-order limiter function developed in [19], we replace the undivided differences as mentioned above to obtain the reconstructions

$$u_{i+\frac{1}{2}}^{(-)} = \bar{u}_i + \frac{1}{2} H_{3L}^{(c)} \left(\Delta x_{i+1} \widetilde{\delta}_{i-\frac{1}{2}}, \Delta_{i-\frac{1}{2}} \ \widetilde{\delta}_{i+\frac{1}{2}} \right) \tag{2.14a}$$

$$u_{i-\frac{1}{2}}^{(+)} = \bar{u}_i - \frac{1}{2} H_{3L}^{(c)} \left(\Delta x_{i-1} \widetilde{\delta}_{i+\frac{1}{2}}, \Delta_{i+\frac{1}{2}} \ \widetilde{\delta}_{i-\frac{1}{2}} \right). \tag{2.14b}$$

with the limiter function $H_{3L}^{(c)}$ (2.8) described in Sec. 2.1. The non-equidistant version of the limiter function can be defined as a function $H_{3L,\mathrm{neq}}^{(c)}$, given by

$$\begin{aligned} H_{3L,\mathrm{neq}}^{(c)} \left(\delta_{i-\frac{1}{2}}, \delta_{i+\frac{1}{2}}, \Delta x_i, \Delta x_{i-1}, \Delta x_{i+1} \right) &= H_{3L}^{(c)} \left(\Delta x_{i+1} \frac{\delta_{i-\frac{1}{2}}}{\Delta_{i-\frac{1}{2}}}, \Delta_{i-\frac{1}{2}} \ \frac{\delta_{i+\frac{1}{2}}}{\Delta_{i+\frac{1}{2}}} \right) \\ H_{3L,\mathrm{neq}}^{(c)} \left(\delta_{i+\frac{1}{2}}, \delta_{i-\frac{1}{2}}, \Delta x_i, \Delta x_{i+1}, \Delta x_{i-1} \right) &= H_{3L}^{(c)} \left(\Delta x_{i-1} \frac{\delta_{i+\frac{1}{2}}}{\Delta_{i+\frac{1}{2}}}, \Delta_{i+\frac{1}{2}} \ \frac{\delta_{i-\frac{1}{2}}}{\Delta_{i-\frac{1}{2}}} \right). \end{aligned} \tag{2.15}$$

The decision criterion η (A.2a) for non-uniform meshes reads

$$\eta(\delta_1, \delta_2) = \frac{\sqrt{\delta_1^2 + \delta_2^2}}{\sqrt{\frac{5}{2}\, \alpha\, dx^2}}, \tag{2.16}$$

where δ_1, δ_2 are the same input arguments as for $H_{3L,\mathrm{neq}}^{(c)}$, see Eq. (2.8) and dx is the average mesh size, $dx = (\sum_i \Delta x_i)/\#cells$.

3. Third-Order Limiter in Two Space Dimensions

In this section we extend the third-order limiter function to two space dimensions covering three core areas. First, we discuss how to apply the scheme on uniform Cartesian grids. Then we extend the method to adaptively refined grids. The last part of this section explains how the method can be used on rectangular grids which are non-uniform in x- and y-direction.

3.1. Formulation for 2D Cartesian Grids

In two space dimensions, the domain of interest Ω is divided into non-overlapping cells $C_{i,j} = [x_{i-\frac{1}{2}}, x_{i+\frac{1}{2}}) \times [y_{j-\frac{1}{2}}, y_{j+\frac{1}{2}})$ such that $\Omega = \bigcup_{i,j} C_{i,j}$. Denote by (x_i, y_j) the cell center of cell $C_{i,j}$. The mesh width is given by $\Delta x_i = x_{i+\frac{1}{2}} - x_{i-\frac{1}{2}}$ and $\Delta y_j = y_{j+\frac{1}{2}} - y_{j-\frac{1}{2}}$. Furthermore we denote by $\tilde{\bar{u}}_{i,j}$ the cell–averaged value over cell $C_{i,j}$ and by $\tilde{u}_{i+\frac{1}{2},j}$ and $\bar{u}_{i,j+\frac{1}{2}}$ the interface–averaged values over the corresponding interface. The tilde notation $\tilde{\cdot}$ denotes the average in y-direction and bar $\bar{\cdot}$ denotes the average in x-direction as in the one-dimensional case.

Integrating a hyperbolic conservation law of the form

$$\partial_t u(x,y,t) + \partial_x f(u(x,y,t)) + \partial_y g(u(x,y,t)) = 0 \tag{3.1}$$

over cell $C_{i,j}$ and dividing by the cell area $\Delta x_i \Delta y_j$ yields the two-dimensional semi-discrete flux-differencing finite volume scheme [16]

$$\frac{d\, \tilde{\bar{u}}_{i,j}}{d\, t} = -\frac{1}{\Delta x_i} \left(\tilde{\hat{f}}_{i+\frac{1}{2},j} - \tilde{\hat{f}}_{i-\frac{1}{2},j} \right) - \frac{1}{\Delta y_j} \left(\bar{\hat{g}}_{i,j+\frac{1}{2}} - \bar{\hat{g}}_{i,j-\frac{1}{2}} \right). \tag{3.2}$$

Here, the numerical flux functions $\hat{f}_{i+\frac{1}{2},j}$ and $\hat{g}_{i,j+\frac{1}{2}}$ are approximations to averages of the flux across the corresponding interface [16]

$$\tilde{\hat{f}}_{i+\frac{1}{2},j} \approx \frac{1}{\Delta y_j} \int_{y_{j-\frac{1}{2}}}^{y_{j+\frac{1}{2}}} f(u(x_{i+\frac{1}{2}}, y, t)) dy, \tag{3.3a}$$

$$\bar{\hat{g}}_{i,j+\frac{1}{2}} \approx \frac{1}{\Delta x_i} \int_{x_{i-\frac{1}{2}}}^{x_{i+\frac{1}{2}}} g(u(x, y_{j+\frac{1}{2}}, t)) dx. \tag{3.3b}$$

Similar to other finite volumen methods, applying the scheme described in Sec. 2 in a dimension–by–dimension fashion results in a second order scheme, see e.g. [22][25][4]. In order to remain third-order accurate, we apply the fourth order transformation proposed by Buchmüller and Helzel [4]. Incorporating this so-called order-fix, the scheme can be summarized as follows.

1. Compute the averaged values of the conserved quantities at the cell interfaces in the interior of cell $C_{i,j}$ for all i, j using the one-dimensional limiter functions described in Sec. 2.1

$$\begin{aligned}
\tilde{u}^{(-)}_{i+\frac{1}{2},j} &= \tilde{\bar{u}}_{i,j} + \tfrac{1}{2}\, H(\delta_{i-\frac{1}{2},j}, \delta_{i+\frac{1}{2},j}),\\
\tilde{u}^{(+)}_{i-\frac{1}{2},j} &= \tilde{\bar{u}}_{i,j} - \tfrac{1}{2}\, H(\delta_{i+\frac{1}{2},j}, \delta_{i-\frac{1}{2},j}),\\
\bar{u}^{(-)}_{i,j+\frac{1}{2}} &= \tilde{\bar{u}}_{i,j} + \tfrac{1}{2}\, H(\delta_{i,j-\frac{1}{2}}, \delta_{i,j+\frac{1}{2}}),\\
\bar{u}^{(+)}_{i,j-\frac{1}{2}} &= \tilde{\bar{u}}_{i,j} - \tfrac{1}{2}\, H(\delta_{i,j+\frac{1}{2}}, \delta_{i,j-\frac{1}{2}}).
\end{aligned} \tag{3.4a}$$

   Here, the reconstruction function H can be the unlimited third-order reconstruction H_3, the limiter function $H^{(c)}_{3L}$ or any other third-order limiter fitting the setting. The undivided differences in two-dimensions, $\delta_{i\pm\frac{1}{2},j}, \delta_{i,j\pm\frac{1}{2}}$, are defined similarly to their one-dimensional equivalents, Eq. (2.4),

$$\begin{aligned}
\delta_{i-\frac{1}{2},j} &= \tilde{\bar{u}}_{i,j} - \tilde{\bar{u}}_{i-1,j}\\
\delta_{i+\frac{1}{2},j} &= \tilde{\bar{u}}_{i+1,j} - \tilde{\bar{u}}_{i,j}\\
\delta_{i,j-\frac{1}{2}} &= \tilde{\bar{u}}_{i,j} - \tilde{\bar{u}}_{i,j-1}\\
\delta_{i,j+\frac{1}{2}} &= \tilde{\bar{u}}_{i,j+1} - \tilde{\bar{u}}_{i,j}.
\end{aligned} \tag{3.5}$$

2. Compute point values of the conserved quantities at the center of each cell interface, i.e. compute

$$\begin{aligned}
u^{(\pm)}_{i+\frac{1}{2},j} &= \tilde{u}^{(\pm)}_{i+\frac{1}{2},j} - \frac{1}{24}\left(\tilde{u}^{(\pm)}_{i+\frac{1}{2},j-1} - 2\tilde{u}^{(\pm)}_{i+\frac{1}{2},j} + \tilde{u}^{(\pm)}_{i+\frac{1}{2},j+1}\right),\\
u^{(\pm)}_{i,j+\frac{1}{2}} &= \bar{u}^{(\pm)}_{i,j+\frac{1}{2}} - \frac{1}{24}\left(\bar{u}^{(\pm)}_{i-1,j+\frac{1}{2}} - 2\bar{u}^{(\pm)}_{i,j+\frac{1}{2}} + \bar{u}^{(\pm)}_{i+1,j+\frac{1}{2}}\right).
\end{aligned} \tag{3.6}$$

3. Compute fluxes at the center of the cell interfaces using the computed point values and a consistent numerical flux function, i.e.

$$\hat{f}_{i+\frac{1}{2},j} = \hat{f}(u^{(-)}_{i+\frac{1}{2},j}, u^{(+)}_{i+\frac{1}{2},j}), \quad \hat{g}_{i,j+\frac{1}{2}} = \hat{g}(u^{(-)}_{i,j+\frac{1}{2}}, u^{(+)}_{i,j+\frac{1}{2}}). \tag{3.7}$$

4. Compute averaged values of the numerical flux function, i.e. compute

$$\begin{aligned}
\tilde{\hat{f}}_{i+\frac{1}{2},j} &= \hat{f}_{i+\frac{1}{2},j} + \frac{1}{24}\left(\hat{f}_{i+\frac{1}{2},j-1} - 2\hat{f}_{i+\frac{1}{2},j} + \hat{f}_{i+\frac{1}{2},j+1}\right),\\
\bar{\hat{g}}_{i,j+\frac{1}{2}} &= \hat{g}_{i,j+\frac{1}{2}} + \frac{1}{24}\left(\hat{g}_{i-1,j+\frac{1}{2}} - 2\hat{g}_{i,j+\frac{1}{2}} + \hat{g}_{i+1,j+\frac{1}{2}}\right).
\end{aligned} \tag{3.8}$$

5. Use a high–order accurate Runge–Kutta method for the update in time. In this work, we use the strong stability preserving third–order Runge–Kutta method described by Gottlieb et. al. [10].

This procedure is quite robust even when discontinuities are present. Nevertheless in some situations an unphysical state may be created, therefor we apply a simple limiting as suggested by Buchmüller et. al. [3]. Details on this limiting procedure can be found in the original paper.

Step 1. comprises the reconstruction function $H(\cdot,\cdot)$ that has been described in Sec. 2. For purely smooth solutions, the full third-order reconstruction H_3 can be used in this step. However, when discontinuities are present, the limiter function $H^{(c)}_{3\mathrm{L}}$, Eq. (2.8), is more advisable since oscillations are prevented. In principle, in the dimension-splitting approach described above, $H^{(c)}_{3\mathrm{L}}$ can be applied in the same manner as in one dimension. The decision criterion η (see Appendix Appendix A.1, Eq. (A.2a)) can also be used without any changes in the splitting approach. Only the definition of the radius of the asymptotic region, α (see

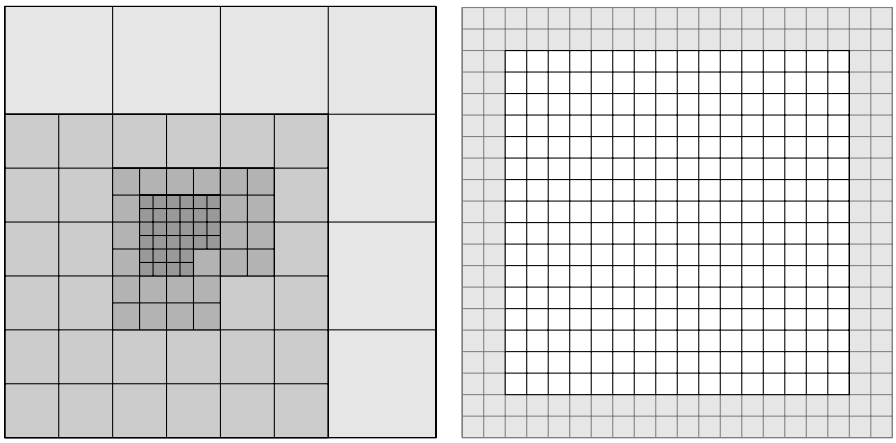

(a) Hierarchy of grid blocks. **(b)** Zoom of a single block.

Fig. 3. (a) Hierarchy of grid blocks of level $2-5$. (b) A single block consisting of 16×16 grid cells, and a layer of two ghost cells.

Appendix Appendix A.1, Eq. (A.2b)) has to be adapted. It is defined as

$$\alpha = \max_{(x,y)\in\Omega\setminus\Omega_d} |\Delta u_0(x,y)| \tag{3.9}$$

in the two-dimensional scheme. Again, Ω is the domain of interest and $\Omega_d \subset \Omega$ the subset containing discontinuities.

3.2. Adaptive Mesh Refinement (AMR)

For computations in two dimensions, we use the parallel AMR framework *Racoon* developed by Dreher and Grauer [7]. Both, the grid adaptivity and the parallelization are based on a block–structure. In a 2-dimensional space, a grid of level ℓ consists of $(2^2)^\ell = 4^\ell$ blocks. Computations can be performed simultaneously on each block and due to the Cartesian grid structure within each block, we can simply apply the method described in Sec. 3.1. A typical block is illustrated in Fig. 3b. The cells in the gray region are ghost cells needed for the communication between the blocks. For refinement a block of level ℓ is replaced by 2^d blocks of level $\ell+1$. These blocks may then be further refined until the maximum refinement level is reached. There are three reasons for refinement.

- Some refinement criteria is met. Here we compute
$$\delta = \frac{|q_{i-1,j} - 2q_{i,j} + q_{i+1,j}| + |q_{i,j-1} - 2q_{i,j} + q_{i,j+1}|}{|q_{i,j}|\Delta x \Delta y} \tag{3.10}$$
for each cell. If δ is bigger than a predefined threshold δ_0, the cell is marked for refinement and therefore the block will be refined.

- Neighbouring blocks are may also refined, so that after refinement the region with the marked cell is surrounded by fine blocks. In 2D for example, if a cell in the upper left part of a block is marked for refinement, then the upper block, the block on the left-hand side, and the block in the upper left diagonal direction will be refined as well.

- Finally the grid needs to be properly nested, that is the level of neighboring blocks is not allowed to differ by more than one. Which may lead to further refinement.

In Fig. 3a, a typical block structure is illustrated. The blocks in this figure are of level $2-5$, where light gray corresponds to 2 and increasing darkness corresponds to increasing refinement level.

As mentioned above, ghost cells are used for communication between blocks and need to be updated in every stage of the time stepping scheme. In most cases this means simply copying the cell–averaged data from the neighboring block. To transfer data from a fine block to a coarse block, the values of the corresponding cells are averaged. Values for the fine block are created by polynomial reconstruction using data of the coarse block. The same is procedure is applied when a block is refined or coarsen again, see [4] for more details.

3.3. Non-Uniform Rectangular 2D Grids

In this section we consider non-uniform two-dimensional meshes. The Cartesian grid cells are transformed into non-uniform cells in x- and y-direction by adding a perturbation to the cell centers (x_i, y_j). In this work we used the transformation

$$\begin{aligned} x_i &\rightarrow x_i + \delta x \sin(c_x \pi x_i), \\ y_j &\rightarrow y_j + \delta y \sin(c_y \pi y_j) \end{aligned} \tag{3.11}$$

with the constants $\delta x, c_x, \delta_y, c_y$, which determine the structure of the mesh. This procedure yields rectangles that are still aligned with the x- and y-axes but exhibit different cell sizes.

In order to apply the numerical schemes presented in the first sections of this paper, we need to adapt the schemes as follows: The general structure of the numerical algorithm for two-dimensional Cartesian grids, introduced in Sec. 3.1, remains the same. We only need to adapt step 1, i.e. the reconstruction of the interface values. The first step of the algorithm for non-uniform grids reads

1. Compute the averaged values of the conserved quantities at the cell interfaces in the interior of cell $C_{i,j}$ for all i, j using the one-dimensional limiter functions for non-uniform grids, described in Sec. 2.2.

$$\begin{aligned} \tilde{u}^{(-)}_{i+\frac{1}{2},j} &= \tilde{\tilde{u}}_{i,j} + \tfrac{1}{2}\, H(\delta_{i-\frac{1}{2},j}, \delta_{i+\frac{1}{2},j}, \Delta x_i, \Delta x_{i-1}, \Delta x_{i+1}), \\ \tilde{u}^{(+)}_{i-\frac{1}{2},j} &= \tilde{\tilde{u}}_{i,j} - \tfrac{1}{2}\, H(\delta_{i+\frac{1}{2},j}, \delta_{i-\frac{1}{2},j}, \Delta x_i, \Delta x_{i+1}, \Delta x_{i-1}), \\ \bar{u}^{(-)}_{i,j+\frac{1}{2}} &= \tilde{\tilde{u}}_{i,j} + \tfrac{1}{2}\, H(\delta_{i,j-\frac{1}{2}}, \delta_{i,j+\frac{1}{2}}, \Delta y_j, \Delta y_{j-1}, \Delta y_{j+1}), \\ \bar{u}^{(+)}_{i,j-\frac{1}{2}} &= \tilde{\tilde{u}}_{i,j} - \tfrac{1}{2}\, H(\delta_{i,j+\frac{1}{2}}, \delta_{i,j-\frac{1}{2}}, \Delta y_j, \Delta y_{j+1}, \Delta y_{j-1}). \end{aligned} \tag{3.12a}$$

   Here, $H = H_{3,\mathrm{neq}}$ or $H = H^{(c)}_{3L,\mathrm{neq}}$. The two-dimensional undivided differences $\delta_{i\pm\frac{1}{2},j}, \delta_{i,j\pm\frac{1}{2}}$, are defined as above, Eq. (3.5) and are adapted to the non-uniform setting as explained in Sec. 2.2.

Steps 2.-5. remain the same, see Sec. 3.1.

4. Numerical examples

In this section we present different numerical examples validating the concepts introduced in Sec. 3. We first prove in Sec. 4.1 that third-order accuracy is obtained on non-equidistant one-dimensional grids. In Sec. 4.3, the vortex evolution performed on a two-dimensional Cartesian mesh shows that also in 2D, the limiter yields third-order accuracy. Then, Sec. 4.2 presents the two-dimensional advection equation on a non-uniform Cartesian mesh. Finally, the double Mach reflection, Sec. 4.4 and the two-dimensional Riemann problem with four shocks show the excellent performance of $H^c_{3\mathrm{L}}$ using AMR.

All simulations were performed using the third-order accurate strong stability preserving Runge-Kutta (SSP-RK3) time integrator developed by Gottlieb et. al. [10].

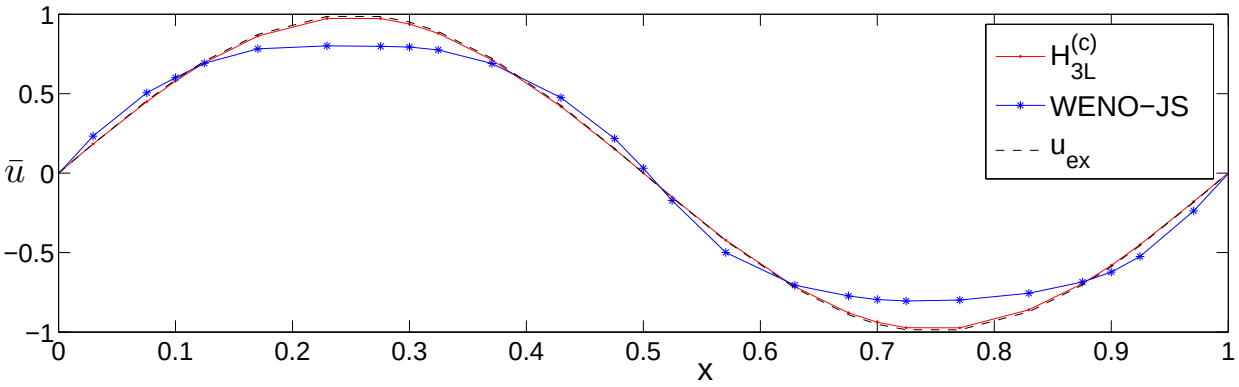

Fig. 4. Comparison of solutions obtained with WENO-JS and H_{3L}^c. Test case (4.1) with $N = 25$ grid cells on $[0, 1]$, CFL 0.95, until time $t_{\text{end}} = 1$.

4.1. Testing the Convergence Order on a Non-Uniform 1D Grid

In this section we want to verify that the extension of the third-order limiter function H_{3L}^c from equidistant to non-equidistant grids still yields third order accurate solutions. Thus, we consider the linear advection equation with smooth initial conditions

$$\begin{cases} u_t + u_x & = 0 \\ u(x,0) & = \sin(2\pi\, x) \end{cases} \tag{4.1}$$

on the domain $[0, 1]$ with periodic boundary conditions. In order to verify the order of convergence we carry out simulations with $N = 25 \times 2^j, j = 0, \ldots, 6$ grid cells with end time $t_{\text{end}} = 1.0$ and CFL number 0.95. Since we are interested in non-equidistant grids, the original grid is perturbed by adding $c_1 \cdot \sin(c_2\, 2\pi\, x_{i+1/2})$ to each cell boundary $x_{i+1/2}$ with some constants $c_1, c_2 \in \mathbb{R}$. In this test case, $c_1 = (10 \cdot c_2)^{-1}$ and $c_2 = 5$ have been applied.

Fig. 4 shows the exact solution as well as the solution obtained with H_{3L}^c on a grid with 25 cells. This solution is compared to the third order WENO method developed by Liu et. al. [17] with the smoothness measure by Jiang and Shu [13]. This scheme is denoted by WENO-JS. The choice of depicting a coarse grid emerges from the fact that the non-equidistant mesh structure is well-visible. Also, the improved solution quality of the limiter function can be best observed on coarse meshes, as for fine grids, all convergent methods look the same.

Finally, to verify that the limiter function is third-order accurate on non-equidistant grids, Table 1a displays the L_1- and L_∞-errors of H_{3L}^c. The corresponding empirical order of convergence (EOC) is obtained by
$\log(err_{j+1}/err_j)/\log(N_j/N_{j+1})$. It can be seen that the limiter function obtains the desired accuracy already on coarse meshes.

Table 1
Errors of $H^c_{3\mathrm{L}}$ in L_1- and L_∞-norm and corresponding empirical order of convergence (EOC).

(a) Perturbed grid by adding $\frac{1}{50}\sin(10\pi\, x_{i+1/2})$ to each cell boundary $x_{i+1/2}$.

Grid	$\|u-u_{ex}\|_1$	EOC	$\|u-u_{ex}\|_\infty$	EOC
25	8.322E-03		1.311E-02	
50	1.347E-03	**2.63**	2.209E-03	**2.57**
100	1.817E-04	**2.89**	2.921E-04	**2.92**
200	2.323E-05	**2.97**	3.663E-05	**3.00**
400	2.920E-06	**2.99**	4.589E-06	**3.00**
800	3.656E-07	**3.00**	5.743E-07	**3.00**

(b) Non-equidistant grid with random cell boundaries.

Grid	$\|u-u_{ex}\|_1$	EOC	$\|u-u_{ex}\|_\infty$	EOC
25	6.412E-03		1.004E-02	
50	7.888E-04	**3.02**	1.240E-03	**3.02**
100	9.844E-05	**3.00**	1.547E-04	**3.00**
200	1.234E-05	**3.00**	1.940E-05	**3.00**
400	1.535E-06	**3.01**	2.411E-06	**3.01**
800	1.930E-07	**2.99**	3.033E-07	**2.99**

4.2. 2D Advection Equation on Non-Uniform Rectangular Grids

This numerical problem verifies the accuracy of the two-dimensional numerical scheme on non-uniform grids, described in Sec. 3.3 and 3.1. We consider the two-dimensional linear advection equation with smooth initial conditions

$$\begin{cases} u_t + a\, u_x + b\, u_y & = 0 \\ u(x,y,0) = u_0(x,y) & = \frac{1}{2}\sin(\pi\, x)\sin(\pi\, y). \end{cases} \tag{4.2}$$

The computational domain is set to $\Omega = [-1,1]\times[-1,1]$ and the non-uniformity is obtained by Eq. (3.11) with $\delta x = 0.1, c_x = 2, \delta y = 0.1, c_y = 1$. Appying an advection speed of either $(a,b) = (1,0)$ or $(a,b) = (1,1)$ and the simulation time $T_{\mathrm{end}} = 2$, the initial condition can be used as exact solution. Thus, the L_1-error of the numerical solution u^n_{ij} can easily be computed as $\|u^n_{ij} - u_0(x_i,y_j)\|_1 = |C_{i,j}|\sum_{i,j}|u^n_{ij} - u_0(x_i,y_j)|$. For the simulation, the CFL condition 0.5 has been imposed and for the decision criterion η of the limiter function $H^{(c)}_{3L,\mathrm{neq}}$, the input value $\alpha = \pi^2$ is obtained by Eq. (3.9). In order to verify the order of convergence, we carry out simulations with $N = \{5\times5, 10\times10, 20\times20, 30\times30, 50\times50\}$ grid cells. The mesh with 30×30 grid cells, perturbed as described above, is depicted in Fig. 5a and the solution obtained using $H^{(c)}_{3L}$is shown in Fig. 5b. The L_1-errors and the corresponding empirical orders of convergence are given in Table 2. The errors for advection speed $(1,0)$ are by a mean factor of 0.7 better than the errors of the solutions advected in diagonal direction $(1,1)$. Nevertheless, both simulations yield third order accuracy, see Table 2

Table 2
Errors of $H^c_{3\mathrm{L}}$ in the L_1-norm and corresponding empirical order of convergence (EOC).

Grid	adv. in x-dir. $\|u-u_{ex}\|_1$	EOC	adv. in diag. dir. $\|u-u_{ex}\|_1$	EOC
5×5	3.886E-01		5.671E-01	
10×10	1.536E-01	**1.34**	2.503E-01	**1.18**
20×20	2.621E-02	**2.55**	6.626E-02	**1.92**
30×30	8.304E-03	**2.83**	2.088E-02	**2.85**
50×50	1.856E-04	**2.93**	4.410E-03	**3.04**

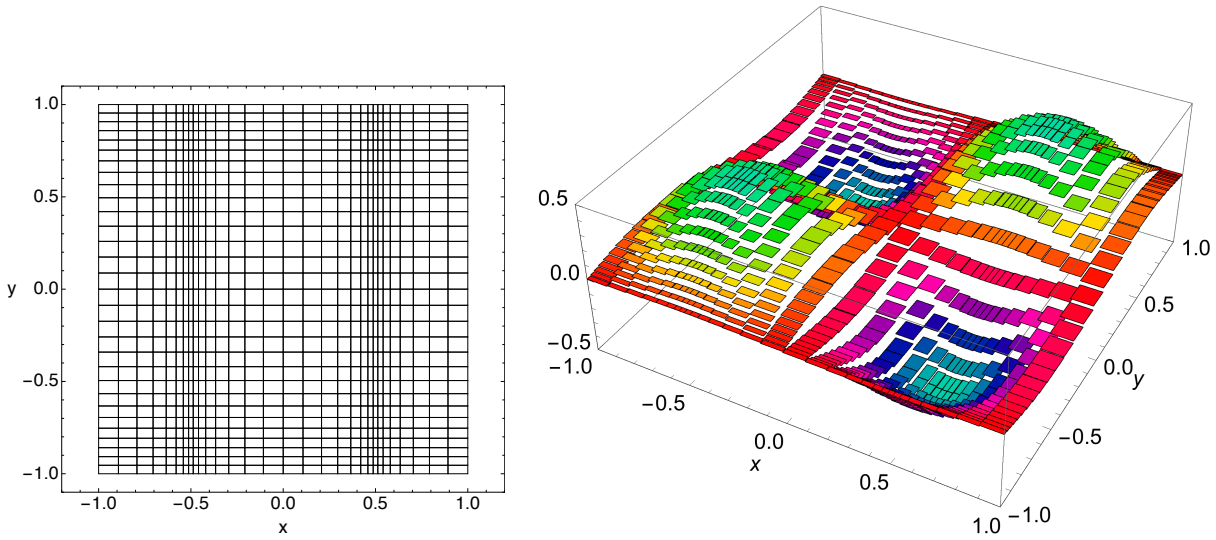

(a) Non-uniform mesh with 30×30 grid cells, obtained by Eq. (3.11) with $\delta x = \delta y = 0.1, c_x = 2, c_y = 1$.

(b) Solution obtained with $H_{3L}^{(c)}$.

Fig. 5. Computation of Eq. (4.2) on a non-uniform mesh with 30×30 grid cells.

4.3. 2D Vortex Evolution

This problem, originally proposed by Hu [12], describes a two-dimensional vortex evolution on the periodic domain $[-7, 7] \times [-7, 7]$, where the flow is described by the Euler equations. The initial data consists of a mean flow $\rho = u = v = p = 1$, perturbed by

$$\begin{pmatrix} \delta\rho \\ \delta u \\ \delta v \\ \delta p \end{pmatrix} = \begin{pmatrix} (1+\delta T)^{1/(\gamma-1)} - 1 \\ -y\frac{\sigma}{2\pi}e^{0.5(1-r)} \\ x\frac{\sigma}{2\pi}e^{0.5(1-r)} \\ (1+\delta T)^{\gamma/(\gamma-1)} - 1 \end{pmatrix}. \tag{4.3}$$

The perturbations in density and pressure are expressed in terms of perturbation in temperature, δT, given by

$$\delta T = -\frac{(\gamma-1)\sigma^2}{8\gamma\pi^2}e^{1-r^2}, \tag{4.4}$$

with $r^2 = x^2 + y^2$, the adiabatic index $\gamma = 1.4$, and the vortex strength $\sigma = 5$. The initial data is also used as a reference solution at time $t = 14$, where it agrees with the exact solution. For the limiter function we need to compute the radius of the asymptotic region, α, given by Eq. (3.9). In this case, $\alpha = 7.9$ is used for the simulation. By applying the method on a two-dimensional Cartesian grid, as suggested in Sec. 3.1, we obtain the full third order, as shown in Table 3. The results compare well with the third-order WENO-Z3 implementation developed by Borges et. al. [2] and further improved by Don and Borges [6]. Both schemes, the $H_{3L}^{(c)}$ limiter function and WENO-Z3, are implemented following the algorithm described in Sec. 3.1.

Table 3
Results for the Vortex evolution problem an a uniform grid.

Grid	WENO-Z3 $\|\rho - \rho_{ex}\|_1$	EOC	$H_{3L}^{(c)}$ $\|\rho - \rho_{ex}\|_1$	EOC
64×64	1.284E-03		1.186E-03	
128×128	2.302E-04	**2.48**	2.281E-04	**2.38**
256×256	3.125E-05	**2.88**	3.120E-05	**2.87**
512×512	3.955E-06	**2.98**	3.953E-06	**2.98**
1024×1024	4.954E-07	**3.00**	4.954E-07	**3.00**
2048×2048	6.194E-08	**3.00**	6.194E-08	**3.00**

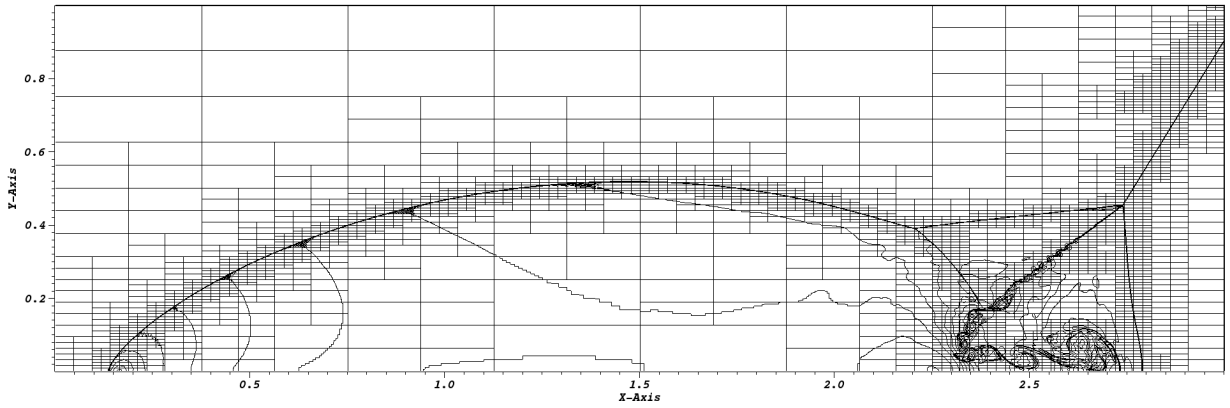

Fig. 6. AMR computation of the Double Mach Reflection problem computed with $H_{3L}^{(c)}$. The grid resolution corresponds to a grid with 288×96 mesh cells on the coarsest level and up to 4608×1536 mesh cells on the finest level.

4.4. Double Mach Reflection

In this section we apply the limiter function on a Cartesian grid with AMR, as described in Sec. 3.2. The test case consists of the double Mach reflection problem proposed by Woodward and Colella [24]. It describes a Mach 10 shock reflection off a 30–degree wedge. The computational domain is the rectangle $[0, 3] \times [0, 1]$. To obtain the same resolution for both, the $x-$ and $y-$direction, each block contains 36×12 mesh cells. We set level 3 as the coarsest level and allow up to 4 additional refinements, thus the finest level corresponds to a discretization with 4608×1536 mesh cells. The refinement threshold is set to $\delta_0 = 2000$. Due to the constant initial date, α turns out to be 0, cf. Eq. (3.9). Therefore, the combined limiter function $H_{3L}^{(c)}$, Eq. (2.8), reduces to $H_{3\mathrm{L}}$, see Eq. (A.1).

Fig. 6 shows the result of the simulation using the third-order limiter function H_{3L} at time $t_{end} = 0.2$, including the block structure.

A close–up view of the Mach stem region is shown in Fig. 7. The computations were performed with four (Fig. 7a and 7b) and five (Fig. 7c and 7d) levels of refinement. For comparison, we also show the results of a third-order WENO-Z reconstruction on the left hand side. In direct comparison the $H_{3L}^{(c)}$ scheme produces more roll ups in the inner region. This is a desired feature since the slip line is physically instable, indicating that the scheme with $H_{3L}^{(c)}$introduces less numerical viscosity than WENO-Z3.

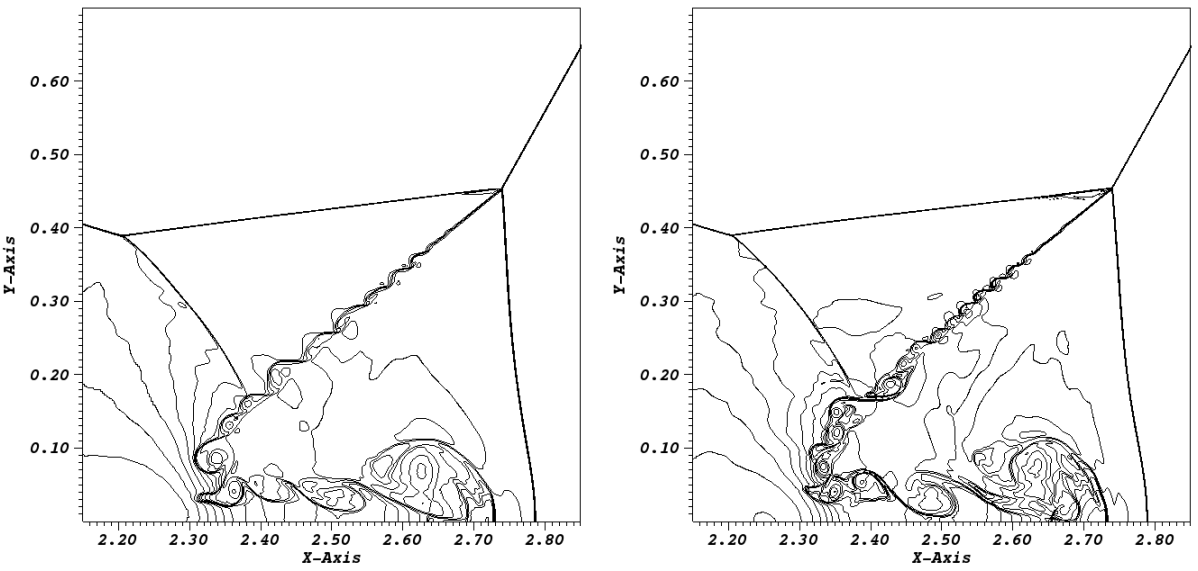

(a) Computed with WENO-Z3 on an adaptive grid of level 3–7.

(b) Computed with $H_{3L}^{(c)}$ on an adaptive grid of level 3–7.

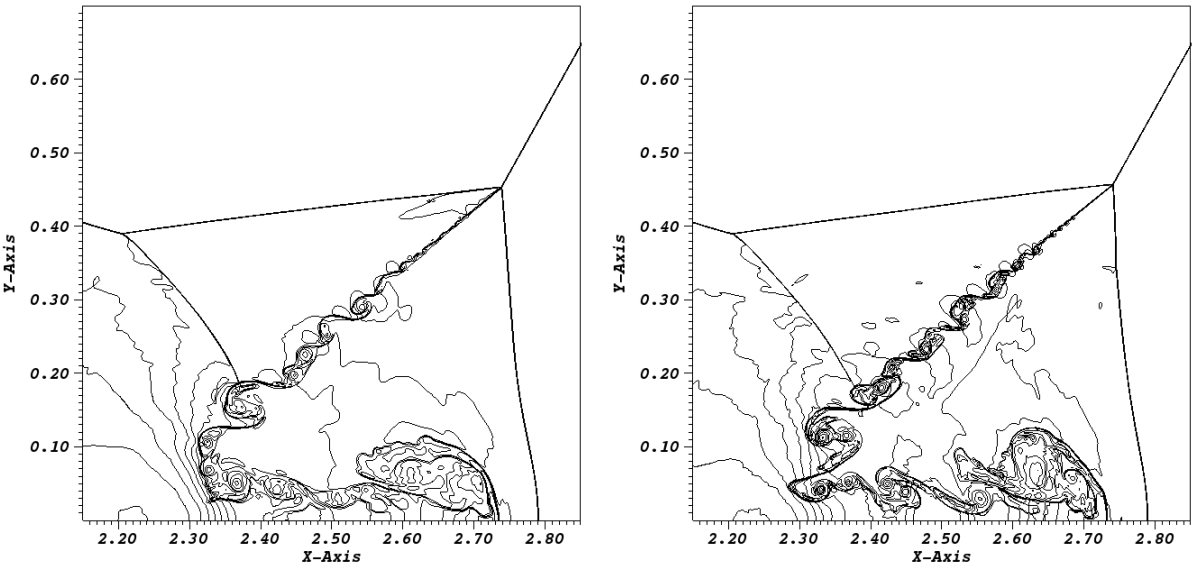

(c) Computed with WENO-Z3 on an adaptive grid of level 3–8.

(d) Computed with $H_{3L}^{(c)}$ on an adaptive grid of level 3–8.

Fig. 7. AMR computation of the Double Mach Reflection problem.

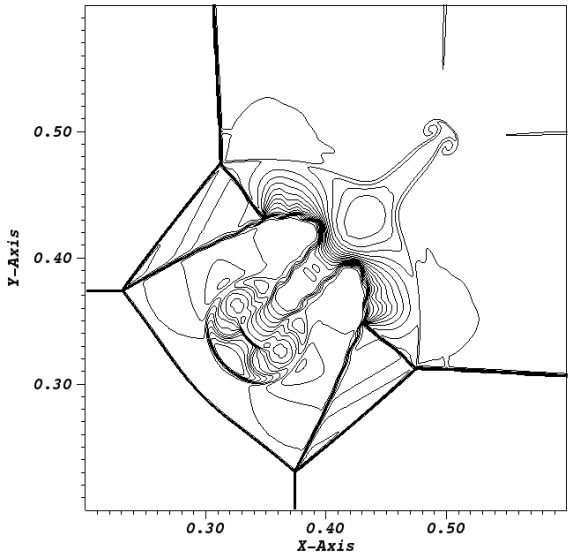

(a) Computed with WENO-Z3 on a uniform grid. 1024×1024 mesh cells.

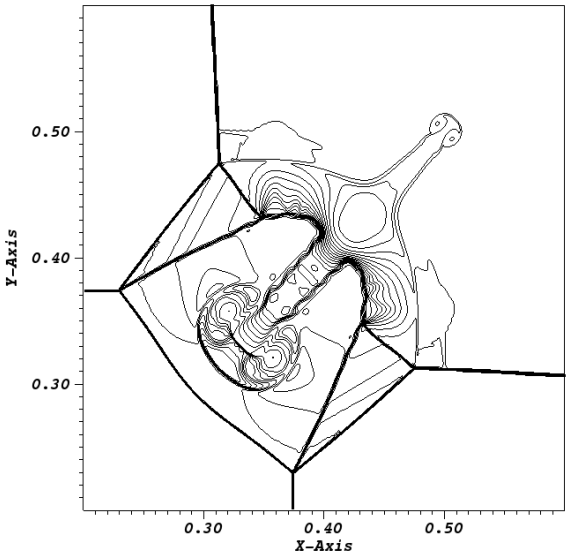

(b) Computed with $H_{3L}^{(c)}$ on a uniform grid. 1024×1024 mesh cells.

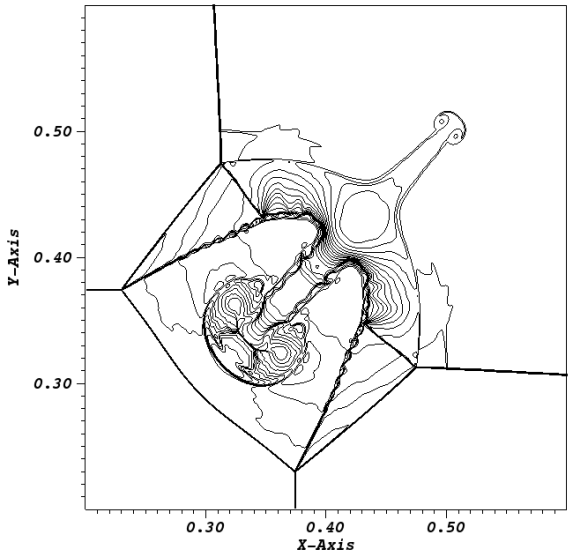

(c) Computed with WENO-Z3 on a uniform grid. 2048×2048 mesh cells.

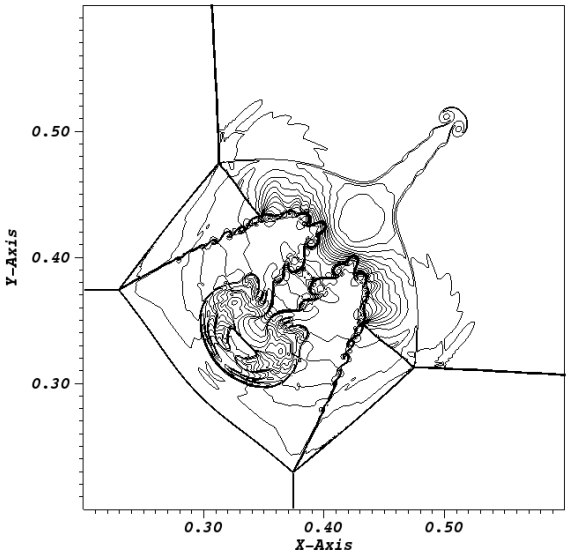

(d) Computed with $H_{3L}^{(c)}$ on a uniform grid. 2048×2048 mesh cells.

Fig. 8. Results of the 2D Rimann problem at final time $t_{end} = 0.3$.

4.5. 2D Riemann Problem

The next testcase we consider is a configuration of four interacting shocks in the domain $[0,1]^2$. The initial values have the form

$$(\rho,p,u,v)(x,y,0) = \begin{cases} (1.5,1.5,0.0,0.0) & x>0.5, y>0.5 \\ (0.5323,0.3,1.2060,0.0) & x<0.5, y>0.5 \\ (0.1380,0.029,1.2060,1.2060) & x<0.5, y<0.5 \\ (0.5323,0.3,0.0,1.2060) & x>0.5, y<0.5 \end{cases} . \tag{4.5}$$

This testcase was originally proposed by Schulz-Rinne [20, 21] along with several other configurations of 2D Riemann problems. Due to the constant initial data we set here $\alpha = 0$ for the limiter $H_{3L}^{(c)}$, see Appendix A.1.

Fig. 8 shows the results at final time $t_{end} = 0.3$. The results obtained by applying the limiter function $H_{3L}^{(c)}$are compared to results computed with the third-order WENO-Z reconstruction. As for the double Mach reflection, Sec. 4.4, the scheme with $H_{3L}^{(c)}$introduces less numerical viscosity than WENO-Z3.

5. Conclusion

In this work we have extended the recently proposed third-order limiter function $H_{3L}^{(c)}$ [19] from one-dimensional equidistant grids to non-uniform and Cartesian AMR meshes in two space dimensions. For the reconstruction of interface values, the presented limiter function takes into account the smallest possible stencil for reaching third-order accuracy. Thus, in one space dimension the reconstruction necessitates three cell mean values and in two dimensions five cells.

For the limiter to be applicable to one dimensional non-equidistant grids, the undivided differences $\delta_{i-1/2} = \bar{u}_i - \bar{u}_{i-1}$ and $\delta_{i+1/2} = \bar{u}_{i+1} - \bar{u}_i$ have been adapted to be meaningful again. The resulting expressions are closely related to the smoothness indicators by Jiang and Shu [13]. A numerical test case verifies that the resulting scheme yields the desired third-order accuracy.

For the two dimensional test cases, the popular approach of dimension splitting has been applied. In order to use this method without loss of third-order accuracy, we use the order-fix developed in [4]. Here, the scheme has first been extended to Cartesian grids, then we showed that it can be incorporated in a scheme with adaptive mesh refinement and also two-dimensional, non-uniform rectangular grids have been proven to yield third-order accurate solutions.

The resulting scheme has been tested on a number of numerical examples and shows the desired third-order accuracy. We also compared the limiter function to the third-order WENO-Z3 reconstruction [2, 6] and obtain equally good results. $H_{3L}^{(c)}$seems to introduce less viscosity into the scheme, thus being able to better reproduce the physically instable details of the double Mach reflection problem.

Appendix A. Appendix

Appendix A.1. Brief Summary of $H_{3L}^{(c)}$ on Uniform-Grids

In this section we want to recall the third-order limiter function developed in [19]. In one space dimension on equidistant grids it reads

$$\begin{aligned} H_{3\mathrm{L}}(\delta_{i-\frac{1}{2}},\delta_{i+\frac{1}{2}}) = \operatorname{sgn}(\delta_{i+\frac{1}{2}})\ \max(0, \min(\operatorname{sgn}(\delta_{i+\frac{1}{2}})\, H_3, \max(-\operatorname{sgn}(\delta_{i+\frac{1}{2}})\delta_{i-\frac{1}{2}}, \\ \min(2\operatorname{sgn}(\delta_{i+\frac{1}{2}})\delta_{i-\frac{1}{2}}, \operatorname{sgn}(\delta_{i+\frac{1}{2}})\, H_3, 1.5|\delta_{i+\frac{1}{2}}|)))). \end{aligned} \tag{A.1}$$

As described in [19], there exist cases, where the limiter function $H_{3\mathrm{L}}$ is unable to distinguishing between smooth extrema and discontinuities due to the constraint of using three cells only. Therefore, the decision

criterion η was introduced, which is able to distinguish between smooth extrema and discontinuities in most cases. The switch function is defined by

$$\eta = \eta(\delta_{i-\frac{1}{2}}, \delta_{i+\frac{1}{2}}) = \frac{\sqrt{(\delta_{i-\frac{1}{2}})^2 + (\delta_{i+\frac{1}{2}})^2}}{\sqrt{\frac{5}{2}}\,\alpha\,\Delta x^2}, \tag{A.2a}$$

where α denotes the maximum second derivative of the initial conditions

$$\alpha \equiv \max_{x \in \Omega \setminus \Omega_d} |u_0''(x)|. \tag{A.2b}$$

Here, Ω is the computational domain and $\Omega_d \subset \Omega$ the subset containing discontinuities. This means that the maximum second derivative is only considered in smooth parts of the domain. With the switch function η, the combined limiter function reads

$$H_{3\mathrm{L}}^{(c)}(\delta_{i-\frac{1}{2}}, \delta_{i+\frac{1}{2}}) = \begin{cases} H_3(\delta_{i-\frac{1}{2}}, \delta_{i+\frac{1}{2}}) & \text{if } \eta < 1 \\ H_{3\mathrm{L}}(\delta_{i-\frac{1}{2}}, \delta_{i+\frac{1}{2}}) & \text{if } \eta \geq 1. \end{cases} \tag{A.3}$$

Note that for performance reasons, instead of computing η in every cell by using (A.3) we precompute

$$\tau = \frac{5}{2}\left(\alpha \Delta x^2\right)^2$$

and use

$$H_{3\mathrm{L}}^{(c)}(\delta_{i-\frac{1}{2}}, \delta_{i+\frac{1}{2}}) = \begin{cases} H_3(\delta_{i-\frac{1}{2}}, \delta_{i+\frac{1}{2}}) & \text{if } \delta_{i-\frac{1}{2}}^2 + \delta_{i+\frac{1}{2}}^2 < \tau \\ H_{3\mathrm{L}}(\delta_{i-\frac{1}{2}}, \delta_{i+\frac{1}{2}}) & \text{if } \delta_{i-\frac{1}{2}}^2 + \delta_{i+\frac{1}{2}}^2 \geq \tau \end{cases} \tag{A.4}$$

instead of Eq. (A.3). This leads to a significant reduction of computational time.

Appendix A.2. Derivation of the Full-Third-Order Reconstruction on Non-Equidistant Grids

The quadratic polynomial $p_i(x)$ which satisfies

$$\frac{1}{\Delta x_{i+\ell}} \int_{x_{i-\frac{1}{2}+\ell}}^{x_{i+\frac{1}{2}+\ell}} p_i(x)dx = \bar{u}_{i+\ell}, \quad \ell \in \{-1, 0, 1\}$$

is given by

$$p_i(x) = a\,(x - x_i)^2 + b\,(x - x_i) + c \tag{A.5a}$$

with

$$a = \frac{1}{2}\frac{\frac{\Delta x_i+\Delta x_{i+1}}{2}(u_{i-1}-u_i)+\frac{\Delta x_i+\Delta x_{i-1}}{2}(u_{i+1}-u_i)}{\left(\frac{\Delta x_i+\Delta x_{i-1}}{2}\right)\left(\frac{\Delta x_i+\Delta x_{i+1}}{2}\right)\Delta_i}, \tag{A.5b}$$

$$\begin{aligned} b = {} & \frac{u_i(\Delta x_{i+1}-\Delta x_{i-1})(2\Delta_i+3\Delta x_i)}{\left(\frac{\Delta x_i+\Delta x_{i-1}}{2}\right)\left(\frac{\Delta x_i+\Delta x_{i+1}}{2}\right)\Delta_i} \\ & - \frac{\frac{2}{3}u_{i-1}\left(\frac{\Delta x_i+\Delta x_{i+1}}{2}\right)\left(2\frac{(\Delta x_i+\Delta x_{i+1})}{2}+\Delta x_{i+1}\right)}{\left(\frac{\Delta x_i+\Delta x_{i-1}}{2}\right)\left(\frac{\Delta x_i+\Delta x_{i+1}}{2}\right)\Delta_i} \\ & + \frac{\frac{2}{3}u_{i+1}\left(\frac{\Delta x_i+\Delta x_{i-1}}{2}\right)\left(2\frac{(\Delta x_i+\Delta x_{i-1})}{2}+\Delta x_{i-1}\right)}{\left(\frac{\Delta x_i+\Delta x_{i-1}}{2}\right)\left(\frac{\Delta x_i+\Delta x_{i+1}}{2}\right)\Delta_i}, \end{aligned} \tag{A.5c}$$

$$\begin{aligned} c = {} & \frac{u_i\left(\Delta x_i\left(6\Delta x_i^2+9\Delta x_i(\Delta x_{i-1}+\Delta x_{i+1})+4(\Delta x_{i-1}+\Delta x_{i+1})^2\right)+4\Delta x_i\Delta x_{i-1}\Delta x_{i+1}\right)}{4(\Delta x_i+\Delta x_{i-1})(\Delta x_i+\Delta x_{i+1})3\Delta_i} \\ & + \frac{4\Delta x_{i-1}\Delta x_{i+1}(\Delta x_{i-1}+\Delta x_{i+1})u_i-\Delta x_i^2(u_{i-1}(\Delta x_i+\Delta x_{i+1})+u_{i+1}(\Delta x_i+\Delta x_{i-1}))}{4(\Delta x_i+\Delta x_{i-1})(\Delta x_i+\Delta x_{i+1})3\Delta_i}. \end{aligned} \tag{A.5d}$$

Evaluating this polynomial at $x_{i+\frac{1}{2}}$ and rearranging yields the formulation

$$u_{i+\frac{1}{2}}^{(-)} = \bar{u}_i + \tfrac{1}{2}\, H_{3,\mathrm{neq}}\left(\delta_{i-\frac{1}{2}}, \delta_{i+\frac{1}{2}}, \Delta x_i, \Delta x_{i-1}, \Delta x_{i+1}\right)$$

with $H_{3,\mathrm{neq}}$ given by

$$H_{3,\mathrm{neq}}\left(\delta_{i-\frac{1}{2}}, \delta_{i+\frac{1}{2}}, \Delta x_i, \Delta x_{i-1}, \Delta x_{i+1}\right) = \frac{\Delta x_i}{\Delta_i}\frac{1}{3}\left(2\frac{\Delta_{i-\frac{1}{2}}}{\Delta_{i+\frac{1}{2}}}\delta_{i+\frac{1}{2}} + \frac{\Delta x_{i+1}}{\Delta_{i-\frac{1}{2}}}\delta_{i-\frac{1}{2}}\right)$$

with the abbreviations

$$\Delta_i = \frac{\Delta x_{i-1}+\Delta x_i+\Delta x_{i+1}}{3},\ \ \Delta_{i-\frac{1}{2}} = \frac{\Delta x_{i-1}+\Delta x_i}{2},\ \ \Delta_{i+\frac{1}{2}} = \frac{\Delta x_i+\Delta x_{i+1}}{2}.$$

Evaluating and rearranging $p_i(x_{i-\frac{1}{2}})$ yields

$$u_{i-\frac{1}{2}}^{(+)} = \bar{u}_i - \tfrac{1}{2}\, H_{3,\mathrm{neq}}\left(\delta_{i+\frac{1}{2}}, \delta_{i-\frac{1}{2}}, \Delta x_i, \Delta x_{i+1}, \Delta x_{i-1}\right)$$

with the same reconstruction function $H_{3,\mathrm{neq}}$. Note however, that the order of the arguments has changed in this case leading to

$$H_{3,\mathrm{neq}}\left(\delta_{i+\frac{1}{2}}, \delta_{i-\frac{1}{2}}, \Delta x_i, \Delta x_{i+1}, \Delta x_{i-1}\right) = \frac{\Delta x_i}{\Delta_i}\frac{1}{3}\left(2\frac{\Delta_{i+\frac{1}{2}}}{\Delta_{i-\frac{1}{2}}}\delta_{i-\frac{1}{2}} + \frac{\Delta x_{i-1}}{\Delta_{i+\frac{1}{2}}}\delta_{i+\frac{1}{2}}\right).$$

References

References

[1] Artebrant, R. and Schroll, H. J. (2006). Limiter-free third order logarithmic reconstruction. *SIAM Journal on Scientific Computing*, 28(1):359–381.

[2] Borges, R., Carmona, M., Costa, B., and Don, W. (2008). An improved weighted essentially non-oscillatory scheme for hyperbolic conservation laws. *J. Comput. Phys.*, 227(6):3191 – 3211.

[3] Buchmüller, P., Dreher, J., and Helzel, C. (2016). Finite volume WENO methods for hyperbolic conservation laws on Cartesian grids with adaptive mesh refinement. *Appl. Math. Comput.*, 272, Part 2:460 – 478. Recent Advances in Numerical Methods for Hyperbolic Partial Differential Equations.

[4] Buchmüller, P. and Helzel, C. (2014). Improved accuracy of high-order WENO finite volume methods on Cartesian grids. *J. Sci. Comput.*, 61(2):343–368.

[5] Čada, M. and Torrilhon, M. (2009). Compact third order limiter functions for finite volume methods. *J. Comput. Phys.*, 228(11):4118–4145.

[6] Don, W. and Borges, R. (2013). Accuracy of the weighted essentially non-oscillatory conservative finite difference schemes. *J. Comput. Phys.*, 250:347 – 372.

[7] Dreher, J. and Grauer, R. (2005). Racoon: A parallel mesh-adaptive framework for hyperbolic conservation laws. *Parallel Comput.*, 31(8–9):913 – 932.

[8] Dubois, F. (1990). Nonlinear interpolation and total variation diminishing schemes. Technical report.

[9] Godunov, S. K. (1959). A difference scheme for the numerical computation of a discontinuous solution of the hydrodynamic equations. *Math. Sbornik*, 47:271–306.

[10] Gottlieb, S., Shu, C.-W., and Tadmor, E. (2001). Strong stability preserving high order time discretization methods. *SIAM Review*, 43(1):89–112.

[11] Harten, A., Engquist, B., Osher, S., and Chakravarthy, S. (1987). Uniformly high order accurate essentially non-oscillatory schemes. III. *J. Comput. Phys.*, 71(2):231–303.

[12] Hu, C. and Shu, C.-W. (1999). Weighted essentially non-oscillatory schemes on triangular meshes. *Journal of Computational Physics*, 150(1):97 – 127.

[13] Jiang, G.-S. and Shu, C.-W. (1996). Efficient implementation of weighted ENO schemes. *J. Comput. Phys.*, 126(1):202–228.

[14] Kriel, A. (2017). Error analysis of flux limiter schemes at extrema. *J. Comput. Phys.*, 328:371–386.

[15] Le Veque, R. J. (1992). *Numerical methods for conservation laws*. Birkhäuser, second edition.

[16] Le Veque, R. J. (2002). *Finite volume methods for hyperbolic problems*. Cambridge University Press, first edition.

[17] Liu, X.-D., Osher, S., and Chan, T. (1994). Weighted essentially non-oscillatory schemes. *J. Comput. Phys.*, 115:200–212.

[18] Marquina, A. (1994). Local piecewise hyperbolic reconstruction of numerical fluxes for nonlinear scalar conservation laws. *SIAM J. Sci. Comput.*, 15:892–915.

[19] Schmidtmann, B., Seibold, B., and Torrilhon, M. (2016). Relations between WENO3 and third-order limiting in finite volume methods. *J. Sci. Comput.*, 68(2):624–652.

[20] Schulz-Rinne, C. (1993). Classification of the Riemann problem for two-dimensional gas dynamics. *SIAM Journal on Mathematical Analysis*, 24(1):76–88.

[21] Schulz-Rinne, C., Collins, J., and Glaz, H. (1993). Numerical solution of the Riemann problem for two-dimensional gas dynamics. *SIAM Journal on Scientific Computing*, 14(6):1394–1414.

[22] Shu, C.-W. (2009). High order weighted essentially nonoscillatory schemes for convection dominated problems. *SIAM Review*, 51(1):82–126.

[23] van Leer, B. (1979). Towards the ultimate conservative difference scheme V. A second-order sequel to Godunov's method. *J. Comput. Phys.*, 32:101–136.

[24] Woodward, P. and Colella, P. (1984). The numerical simulation of two-dimensional fluid flow with strong shocks. *J. Comput. Phys.*, 54(1):115 – 173.

[25] Zhang, R., Zhang, M., and Shu, C.-W. (2011). On the order of accuracy and numerical performance of two classes of finite volume WENO schemes. *Communications in Computational Physics*, 9(3):807–827.